Nanoscale

Upconversion luminescence and blackbody radiation in tetragonal YSZ co-doped with Tm^{3+} and Yb^{3+}

Journal:	*Nanoscale*
Manuscript ID	NR-ART-06-2015-004052.R1
Article Type:	Paper
Date Submitted by the Author:	18-Sep-2015
Complete List of Authors:	Soares, Maria Rosa; University of Aveiro, Department of Physics- I3N Ferro, Marta; Universidade de Aveiro, Departamento de Eng. de Materiais e Cerâmica & CICECO Costa, Florinda; University of Aveiro, Department of Physics Monteiro, Teresa; University of Aveiro, Department of Physics

Journal Name

ARTICLE

Upconversion luminescence and blackbody radiation in tetragonal YSZ co-doped with Tm^{3+} and Yb^{3+}

M.R.N. Soares[a], M. Ferro[b], F. M. Costa[a] and T. Monteiro[a]

Received 00th January 20xx,
Accepted 00th January 20xx

DOI: 10.1039/x0xx00000x

www.rsc.org/

Lanthanide doped inorganic nanoparticles with upconversion luminescence are of upmost importance for biomedical applications, solid state lighting and photovoltaics. In this work we studied the downshifted luminescence, upconversion luminescence (UCL) and blackbody radiation of tetragonal yttrium stabilized zirconia co-doped with Tm^{3+} and Yb^{3+} single crystals and nanoparticles produced by laser floating zone and laser ablation in liquids, respectively. The photoluminescence (PL) and PL excitation (PLE) were investigated at room temperature (RT). PL spectra exhibit the characteristics lines in UV, blue/green, red and NIR of the Tm^{3+} ($4f^{12}$) under resonant excitation into the high energy $^{2S+1}L_J$ multiplets. Under NIR excitation (980 nm), the samples placed in air display an intense NIR at ~800 nm due to the $^1G_4 \rightarrow {}^3H_5/{}^3H_4 \rightarrow {}^3H_6$ transitions. Additionally, red, blue/green and ultraviolet UCL is observed arising from higher excited $^1G_4$ and $^1D_2$ multiplets. The power excitation dependence of the UCL intensity indicated that 2-3 low energy absorbed photons are involved in the UCL for low power levels, while for high powers, the identified saturation is dependent on the materials size with a enhanced effect on the NPs. The temperature dependence of the UCL was investigated for single crystals and target used in the ablation. An overall increase of the integrated intensity was found to occur between 12 K and the RT. The thermally activated process is described by activation energies of 10 meV and 30 meV for single crystals and targets, respectively. For the NPs, the UCL was found to be strongly sensitive to pressure conditions. In vaccum conditions, instead of the narrow lines of the Tm^{3+}, a wide blackbody radiation was detected, responsible for the change in the emisson colour from blue to orange. This phenomenon is totally reversible when the NPs are placed at ambient pressure. The UCL/blackbody radiation in the nanosized material exhibits non-contact pressure colour-based sensor characteristics. Moreover, tuning the color of the blackbody radiation in the nanoparticles by harvesting the low energy photons into the visible spectral region was found to be possible by adjusting the excitation power, paving the way to further developments of these nanoparticles for lighting and photovoltaic applications.

1. Introduction

Optically activated trivalent lanthanide ions (Ln^{3+}) embedded in inorganic hosts such as fluorides and oxides, constitute a class of materials with high technological importance for lighting applications, including luminescence based sensors. Within the wide range of the investigated oxide materials, zirconia and yttrium stabilized zirconia (YSZ) proved to be suitable hosts for the incorporation of different lanthanide ions which, in the 3+ charge state, present high emission efficiency at room temperature (RT) [1–6]. When doped with Ln^{3+} ions the wide bandgap of YSZ enables the incorporation of a large number of atomic-like energy levels of the ions permitting to tune the intraionic emission from the ultraviolet (UV) to the infrared (IR) [5]. In addition, the phonon energy threshold of this host (~80 meV) represents an advantage, in some cases, by avoiding competitive non-radiative phonon assisted relaxations processes. The high hardness, low thermal conductivity [7,8], high chemical and photo stability together with bioinertness of the YSZ host are also major requirements fulfilled by this oxide material for a wide range of optical applications. With a $4f^{12}$ electron configuration Tm^{3+} has a ladder-like schema of energy levels with a $^3H_6$ ground state and several excited states spanning into the deep UV [9]. When incorporated in wide band gap hosts, optically activated Tm^{3+} ions can exhibit emissions from the UV to the IR due to transitions between the distinct multiplets. One of the most studied emissions of Tm^{3+} ions in inorganic hosts occurs around 2 μm, due to the $^3F_4 \rightarrow {}^3H_6$ transition, and is of special interest for applications in solid state laser technology [10]. Beyond the importance of the IR emission, Tm^{3+} ions provide luminescence in the visible spectral range that are of great importance in other application areas. Particularly, the $^1D_2 \rightarrow {}^3F_4$ and $^1G_4 \rightarrow {}^3H_6$ transitions occurring in the blue spectral region have been widely studied due to their importance in solid state lighting [11]. Moreover, the Tm^{+3} ions levels scheme is suitable for acquiring ultraviolet, blue, red and IR emission as well as to be used as upconverter photon energy. Among others, the latter process is of special

[a] Departamento de Física & I3N, Universidade de Aveiro, 3810-193 Aveiro, Portugal.
[b] Departamento de Eng. de Materiais e Cerâmica & CICECO, Universidade de Aveiro, 3810-193 Aveiro, Portugal.
M.R.N. Soares: E-Mail: rosasoares@ua.pt
See DOI: 10.1039/x0xx00000x

importance for bioimaging, displays, photovoltaics, drug delivery, biosensors and photodynamic therapy [12]. For luminescence based biological applications, including in-vivo procedures, nanosized bio-inert high quality particles dispersed in bio-compatible solutions are required. Particularly, for bioimaging purposes, the $^1G_4 \rightarrow {}^3H_5/{}^3H_4 \rightarrow {}^3H_6$ transitions of Tm^{3+}, located ~800 nm, well within the biological window, is of upmost importance [13]. Such wavelength leads to a deeper light penetration in the biological tissues and a high image contrast due to the absence of the tissue autofluorescence background and reduced light scattering [13]. In recent years, there has been an increasing demand for proper approaches to produce such luminescent nanoparticles (NPs) that can fulfil those requirements. Fluoride-based hosts have been the most used materials for the aforementioned purposes. In fact, due to the low energy phonon cutoff of the hexagonal $NaYF_4$ (β-$NaYF_4$) this material is known as the most efficient material used in blue and green upconversion phosphors among the fluoride hosts [14]. The efficiency is also known to depend on the material crystalline quality and local crystal field around the lanthanides ions. Typically, growth processes such as hydro(solvo)thermal method are required to produce these nanomaterials with high crystalline quality. This synthesis process is more complex and expensive than the ones used for oxides. In such procedure a solvent under pressure and temperatures above its critical point is involved, implying the use of autoclaves during the growth, which constitutes a disadvantage when compared with the synthesis method used for oxide hosts. Moreover, some of the precursors used in the fluorides synthesis are known to be toxic. Furthermore, fluoride materials have limited chemical and thermal stability that can hamper their practical applications [15]. Oxide materials, such those produced in this work by pulsed laser ablation in liquids technique (PLAL) can have high chemical, thermal and photo stability and can be produced by simple and low cost routes.

The PLAL is a versatile method to produce luminescent NPs with those requested requisites. In PLAL technique the NPs could be directly obtained in biocompatible solvents, such as water, in a fast, simple and economic way [16–18]. A high power pulsed laser is used to irradiate a solid target immersed in an appropriated solvent. Depending on the experimental conditions, different chemical species (atoms, ions, clusters, etc.) can be released from the target. As happens in other ablation processes, a plasma plume is formed in the process, but in this case the temperature and pressure inside the plasma plume was reported to be much higher due to the confinement of the plasma by the liquid. As such, the ablated species can nucleate and growth to form very small crystalline NPs [16].

In this work, PLAL and laser floating zone (LFZ) techniques were used to produce YSZ doped with Tm^{3+} (YSZ:Tm) and YSZ co-doped with Tm^{3+} and Yb^{3+} (YSZ:Tm,Yb). The former method was used to produce NPs and the latter single crystals. The laser processed samples were further investigated at RT by optical techniques such as steady state photoluminescence (PL) and PL excitation (PLE). The Stokes-shifted PL and upconversion luminescence (UCL) of the doped samples were analysed and discussed. Particularly, upon 980 nm photon excitation, UCL in the UV, blue/green, red and IR spectral regions was observed, due to the $^1D_2 \rightarrow {}^3H_6$, $^1D_2 \rightarrow {}^3F_4$, $^1G_4 \rightarrow {}^3H_6$, $^1G_4 \rightarrow {}^3F_4$ and $^1G_4 \rightarrow {}^3H_5$ / $^3H_4 \rightarrow {}^3H_6$ transitions of the Tm^{3+}, respectively. Under such excitation conditions, the produced single crystals and NPs exhibit an intense blue light at RT identified by unaided eye. Power excitation dependence of the UCL was studied in order to obtain information about the upconversion mechanisms showing that saturation effects occur for high power levels and are enhanced for the PLAL produced nanosized material. The UCL was found to be a thermally activated process for the single crystals and targets used in the ablation process (produced by the sintering of powders obtained by solution combustion synthesis (SCS)) in the 12 K – RT range. The UCL of the YSZ:Tm,Yb NPs produced by PLAL evidence non-contact colour-sensor characteristics when measured in air and in reduced pressure conditions. The UCL is also strongly dependent on the used power level of the excitation energy. For high incident power levels and reduced pressures a quenching of the narrow atomic-like intraionic lines occurs, being observable a wide blackbody radiation extending into the visible spectral range. Similar anti-Stokes thermal radiation have been recently reported in different doped and undoped hosts [8,19–24] and are of great potential to exploit for visible solid state lighting and photovoltaics as was recently reported by Wang *et al*. [8].

2. Experimental

Tetragonal yttrium stabilized zirconia doped with Tm^{3+} ions (YSZ:Tm) and co-doped with Tm^{3+} and Yb^{3+} ions (YSZ:Tm,Yb) were produced by laser processing techniques. Single crystals of YSZ:Tm and YSZ:Tm,Yb, taken as reference samples for the investigated NPs, were grown by the Laser Floating Zone technique (LFZ). This is a suitable method to grow from the melt crystals with high melting temperature, as is the case of YSZ (~2700 ^oC). The crystals were grown using the same equipment and procedure previously reported by our group for different Ln^{3+} doped YSZ single crystals [5,25,26]. The YSZ:Tm,Yb crystal was grown at 20 mm/h in air at atmospheric pressure. A nominal dopant concentration of 1 mol % Yb and 0.3 mol % Tm was used. A second YSZ crystal doped with 0.3 mol % Tm (YSZ:Tm), grown in the same conditions as the YSZ:Tm,Yb, was used for optical properties comparison. YSZ:Tm,Yb NPs, with the same composition of the co-doped single crystal, were produced by pulsed laser ablation in liquids (PLAL) [27]. For comparison purposes also YSZ:Er,Yb and nominally undoped YSZ were synthesized by PLAL. In the PLAL process, a nanosecond Q-switched pulsed Nd: YAG laser (λ=1064 nm) was focused on the surface of a YSZ:Tm,Yb target immersed in distillate water. The targets were produced by sintering (T = 1350 ^oC, t = 72 h) powders obtained by solution combustion synthesis (SCS) [11,28]. These targets were irradiated with a laser fluence of 1.8 J/cm^2 and with a pulse frequency of 10 Hz. The height of water above the target was 15 mm and the liquid was continuously stirring during the ablation to

allow the produced NPs to spread uniformly in the liquid medium.

The crystalline phases of the produced samples were investigated at RT by Raman spectroscopy, performed in backscattering geometry with a 325 nm laser line excitation in a Horiba JobinYvon HR800 system. The morphology and NPs size distribution were evaluated by transmission electron microscopy (TEM) in a JEOL- 2200FS equipment.

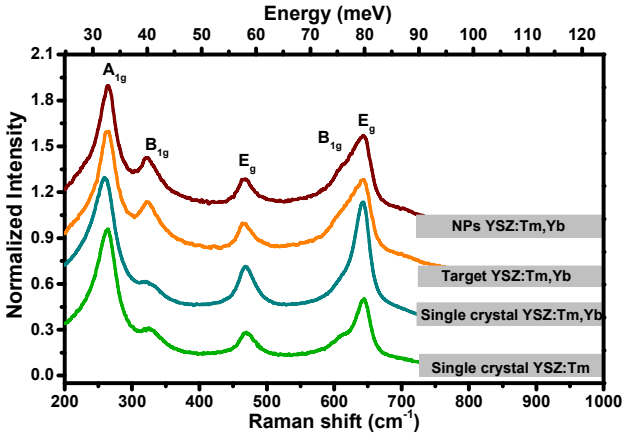

Fig. 1. Room temperature Raman spectra of the produced samples upon 325 nm laser excitation. The spectra were vertically shifted for clarity.

The optical properties of the samples were investigated by steady state PL and PLE. The luminescence of the samples were studied by PL/PLE measurements at RT, recorded in a Fluorolog-3 Horiba Scientific modular equipment with a double additive grating scanning monochromator (2×180 mm, 1200 gr.mm^{-1}) in the excitation and a triple grating iHR550 spectrometer (550 mm, 1200 gr.mm^{-1}) in the emission, coupled to a cooled Hamamatsu R928 photomultiplier. A 450 W Xe lamp was used as excitation source. The PLE was assessed by setting the emission monochromator in the PL energy maxima of the optically active defects and the excitation was scanned to higher energies. The measurements were carried out using front face acquisition geometry, and the spectra were corrected to the spectral responses of the optical components and Xe lamp. The UCL of the samples was studied under infrared excitation using a cw 980 nm laser line, with controllable power output. With the used excitation conditions, the dependence of the UCL intensity with the excitation density and temperature was investigated in order to obtain additional information of the upconversion mechanisms. Additionally, the role of surrounding pressure (air at ambient pressure and vacuum at 10^{-3} mbar) on the UCL properties was exploited by using distinct power levels of the excitation energy.

3. Results and discussion

3.1. Structural and morphological characterization

Figure 1 shows the Raman spectra of the Tm doped and Tm,Yb co-doped YSZ single crystals, targets and NPs. Raman spectroscopy is a powerful tool to distinguish the different crystalline phases of zirconia (monoclinic, tetragonal, cubic) allowing a clear identification of the active vibrational modes for each one of the crystalline phases [29]. Five bands centred at ~264, ~323, ~467, ~612 and ~643 cm^{-1} were identified in the studied spectral region for all the produced samples, corresponding to five of the six vibrational active modes (A_{1g}, B_{1g}, E_g, B_{1g} and E_g, respectively) of the tetragonal phase [29]. The stabilization of the tetragonal phase of zirconia at RT was achieved through the zirconia additivation with yttrium ions.

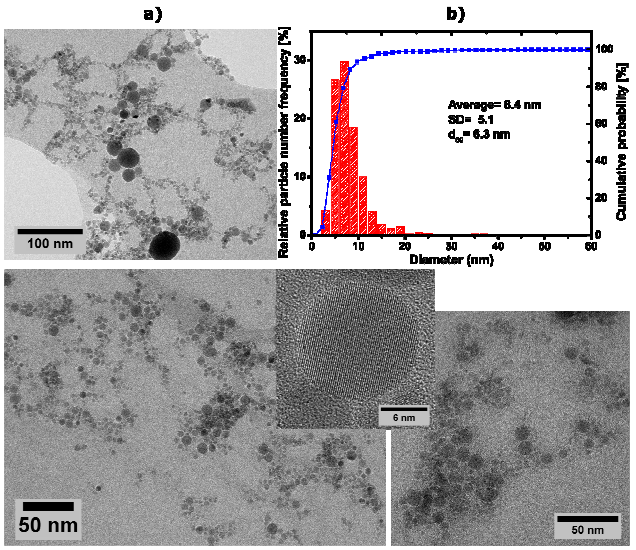

Fig. 2. a) TEM and HRTEM images and b) particle size distribution and respective cumulative probability of the PLAL produced NPs.

The morphology of PLAL produced YSZ:Tm,Yb NPs was analysed by TEM and HRTEM as displayed in Figure 2. The NPs have spherical shape and besides of a few NPs with sizes around 50 and 90 nm, most of NPs have sizes comprising between two to thirty nanometers (Figure 2 a)). The histogram of the particles size distribution and respective cumulative probability (Figure 2 b)) was constructed based on TEM images, using the ImageJ for diameters determination and OriginPro for statistical data analysis. More than 1000 particles were measured for this analysis. The results show that the NPs have an average particle size of 8.4 nm and 98% of the NPs have diameters lower than 23 nm. HRTEM images evidence the high degree of crystallinity of the PLAL produced NPs.

3.2. Optical properties

3.2.1 *Stokes luminescence and photoluminescence excitation* RT PL and PLE. The PL and PLE spectra of the doped and co-doped samples were investigated at RT as shown in Figures 3 and 4.

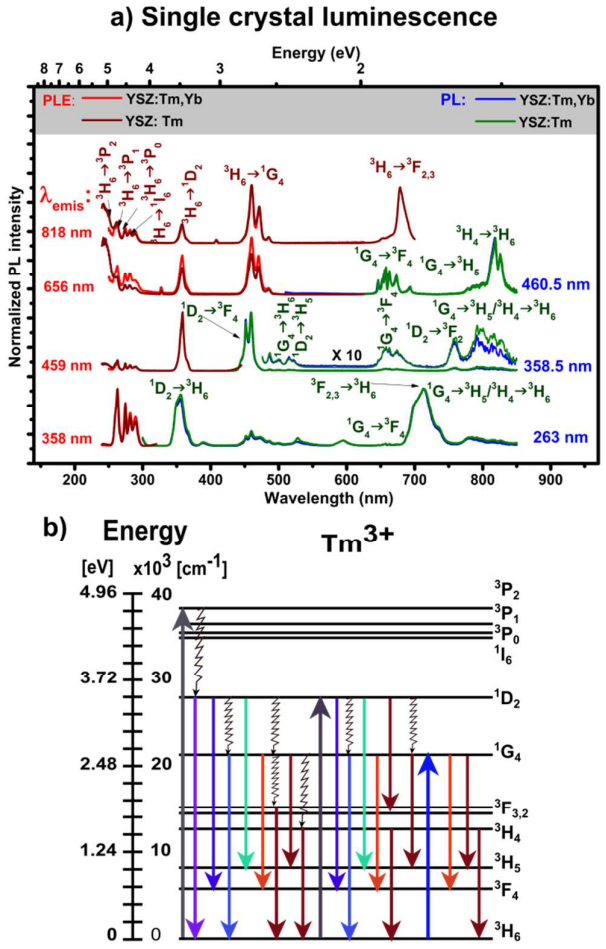

Fig. 3. a) RT PL and PLE spectra of YSZ:Tm and YSZ:Tm,Yb single crystals under resonant excitation into the Tm^{3+} excited multiplets; b) partial energy level diagram of Tm^{3+} free ion with representation of the radiative transition observed in the PL spectra upon resonant excitation into $^3P_2$, $^1D_2$ and $^1G_4$ excited multiplets.

In the case of the YSZ:Tm and YSZ:Tm,Yb single crystals (Figure 3), pumping the samples in the UV by 358.5 nm photons, resonantly with the $^1D_2$ excited multiplet of the Tm^{3+} ions, the PL spectrum is composed by three groups of emitting lines in the blue/green, red and near infrared spectral regions. The intraionic emissions of the Tm^{3+} ions in the blue/green region are due to the $^1D_2 \rightarrow {}^3F_4$, $^1G_4 \rightarrow {}^3H_6$ and $^1D_2 \rightarrow {}^3H_5$ transitions, while the red emission is assigned to the $^1G_4 \rightarrow {}^3F_4$ transition, and the near infrared luminescence to transitions between the $^1D_2 \rightarrow {}^3F_2$, $^1G_4 \rightarrow {}^3H_5$ and $^3H_4 \rightarrow {}^3H_6$ multiplets. The most intense emission occurs in the blue region (~459 nm) and is due to the $^1D_2 \rightarrow {}^3F_4$ transition. The PLE monitored at 459 nm shows that, besides the resonant excitation into the $^1D_2$ multiplet, the ion luminescence can also be observed upon excitation into higher excited states of the Tm^{3+} ($^1I_6$ and $^3P_{2,1,0}$). By exciting the samples into these ^3P_J higher energy multiplets (263 nm), dominant lines at 355 and 712 nm due to the $^1D_2 \rightarrow {}^3H_6$ and $^3F_{2,3} \rightarrow {}^3H_6$ transitions are observed. The enlargement of the lines is due to the overlap of intraionic transitions from distinct multiplets occurring at similar energies. Figure 3 a) also displays the PL spectra under resonant excitation into the $^1G_4$ multiplet showing an enhancement of the near infrared transition arising between the $^1G_4 \rightarrow {}^3H_5$ and $^3H_4 \rightarrow {}^3H_6$ multiplets. The upper spectra, corresponding to the PLE monitored at $^3H_4 \rightarrow {}^3H_6$ transition, indicates that this emission can also be directly excited through the $^3H_6 \rightarrow {}^3F_{2,3}$ absorption. As seen, no significant differences in the PL/PLE spectra were observed for the Tm doped and Tm,Yb co-doped YSZ single crystals.

The PL and PLE of the YSZ:Tm,Yb target and NPs were also investigated and compared with the YSZ:Tm,Yb single crystal discussed above. As can be observed in Figure 4, under resonant excitation into the $^1D_2$ and $^1G_4$ multiplets (358.5 and 460.5 nm, respectively) the RT PL of the target and PLAL NPs exhibits the same intraionic features as the single crystals.

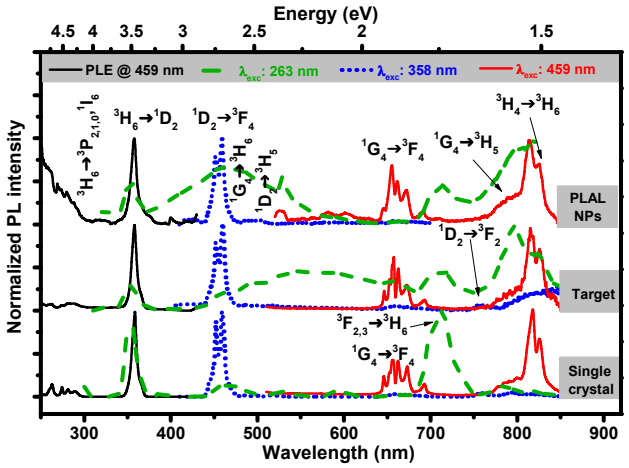

Fig. 4. Comparison of the RT PL and PLE spectra of the YSZ:Tm,Yb ceramic targets, PLAL produced NPs and single crystal.

However, for the excitation at shorter wavelengths, besides the intraionic luminescence, broad emission bands peaked in the blue (~ 465 nm) and orange (~ 570 nm) are observed for the PLAL NPs and targets, respectively. Similar broad bands, likely due to native defects, were previously reported in literature for zirconia host with its peak position and spectral shape dependent on the zirconia crystalline phase and processing conditions [28,30,31]. For the NPs, the RT PLE monitored at 459 nm, in the blue region, assesses both the preferential pathways to populate the ion emission as well as the host defect luminescence. As such, at shorter wavelengths, in the spectral region where the $^3H_6 \rightarrow {}^3P_{2,1,0}, {}^1I_6$ absorption transitions occurs, the identified broad excitation band is likely to be responsible for the population of the intrinsic defect luminescence.

3.2.2 *Anti-Stokes emission*

Upconversion Luminescence (UCL). Upconverted near infrared (NIR) excitation light into visible and ultraviolet photons are of upmost importance for luminescence based sensors, solid state light and photovoltaic applications.

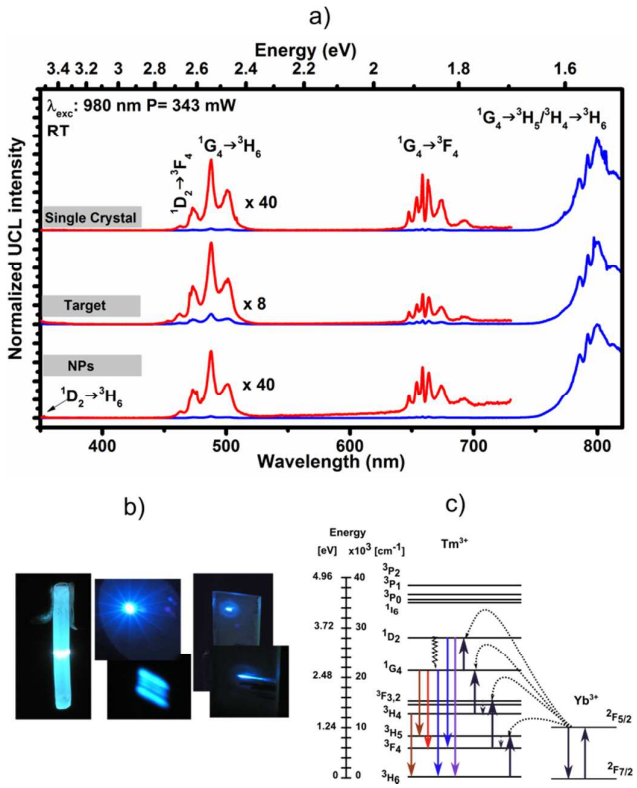

Fig. 5. a) RT PL spectra of the YSZ:Tm,Yb samples in air upon 980 nm photon excitation; b) photos of the single crystal (left), target (middle) and PLAL produced NPs deposited in a sapphire substrate (right) under 980 nm excitation at RT; c) partial energy level diagram of Tm^{3+} and Yb^{3+} with excitation and emission process after 980 nm photon excitation.

The UCL properties of the YSZ:Tm,Yb samples (single crystals, targets and PLAL NPs) were investigated under 980 nm photon energy excitation. The corresponding photon excitation energy is nearly resonant with the absorption energy from the ground state ($^2F_{7/2}$) to the $^2F_{5/2}$ excited multiplet of the Yb^{3+} sensitizer. Figure 5 a) displays the UCL spectra of the YSZ:Tm,Yb single crystal, ceramic target and NPs upon the NIR excitation. The spectra are composed by four groups of emission lines in the UV, blue/green, red and near-infrared spectral region, corresponding to the aforementioned mentioned $^1D_2 \rightarrow {}^3H_6$, $^1D_2 \rightarrow {}^3F_4/{}^1G_4 \rightarrow {}^3H_6$, $^1G_4 \rightarrow {}^3F_4$ and $^1G_4 \rightarrow {}^3H_5/{}^3H_4 \rightarrow {}^3H_6$ transitions of the 3+ charged thulium ions. Comparing the Stokes shifted luminescence discussed in the latter subsection using high energy photons in the excitation (pumping directly the $^1D_2$ multiplet), with the samples luminescence observed by the excitation with 980 nm photons, the intensity ratio of the (blue+red)/NIR emission is much higher in the former case than in the UCL, revealing that the NIR UCL is enhanced by energy transfer from the $^2F_{7/2} \rightarrow {}^2F_{5/2}$ photon absorption of the Yb^{3+} ions. These findings agree well with the model described by Ostermayer *et al.* [32] and Pandozzi *et al.* [33], where the population of the excited energy levels of the Tm^{3+} ions is realized via nonradiative energy transfer and multiphonon decay. After the nonresonant energy transfer $^2F_{7/2}$, $^3H_6 \rightarrow {}^2F_{5/2}$, $^3H_5$ (where the excess in energy, ~1650 cm^{-1}, is assisted by absorption of the YSZ lattice phonons) multiphonon relaxation into the $^3F_4$ multiplet of the Tm^{3+} occurs. This process is followed by a second energy transfer (or via excited state absorption, ESA) to the $^3F_2$ state with subsequent multiphonon relaxation into the $^3H_4$ from where the NIR $^3H_4 \rightarrow {}^3H_6$ emission arises. This route has a high probability to occur due to the low energy difference between the $^3F_2$ and $^3F_3$ levels (~640 cm^{-1}) which can be easily covered by a YSZ host phonon. On the other hand, the subsequent nonradiative relaxation to the $^3H_4$ (displaced from the $^3F_3$ by ~1800 cm^{-1}) requires the assistance of a low number of host phonons [32,33]. Therefore, the intensity of the $^3H_4 \rightarrow {}^3H_6$ transition is higher under the excitation with the low energy photons than when observed by visible or UV excitation. In the latter case a preferential radiative depopulation of the higher energetic levels (separated by the lower lying levels by a high energetic gap) is expected to occur, as also reported by Pandozzi *et al.* [33]. From the UCL spectra it is seen that, at RT, a fourth nonresonant energy transfer occurs in the Tm^{3+} ions involving the population of the $^1D_2$ level (the blue $^1D_2 \rightarrow {}^3F_4$ and the ultraviolet $^1D_2 \rightarrow {}^3H_6$ transitions were identified).

Although in the studied spectral region the infrared emission is the strongest one, in the visible spectral region the blue emission is the most intense and is the responsible for the blue appearance of the samples observed with unaided eye and RT, when pumped with 980 nm light (Figure 5 b)).

It is well documented in the literature (see the review by Auzel [34]) that the UCL occurs upon absorption of low energy photons and could be mediated by distinct mechanisms such as ground and excited state absorption, energy transfer upconversion and photon avalanche. Among the different processes, an in-depth comprehension of the UCL mechanisms for the YSZ:Tm,Yb samples can be obtained through the investigation of the power excitation dependence of the UCL intensity as shown in Figure 6 a), b) and c) for the single crystal, ceramic target and NPs, respectively. As can be identified, within the incident light power range studied, the overall UCL intensity was found to increase with increasing power. However, and as seen in the Figure 6 d), e) and f), where the normalized PL spectra under lower and higher power excitation are compared, such increase in the visible UCL intensity follows distinct trends for single crystals, targets and NPs. For the single crystal, the normalized UCL spectra under lower and higher power excitation are almost overlapped, in all the visible spectral range. This means that the increase in the power pump results in an almost equal increase in the intensity of the blue and red UCL. However, it is possible to observe that for the higher power excitation the ratio between the red and blue luminescence slightly increases comparatively to the lower power excitation. Moreover, looking to the blue emission, a slight change in the intensity ratio between the emissions arising from the different energy levels is also observed with the increase in power excitation.

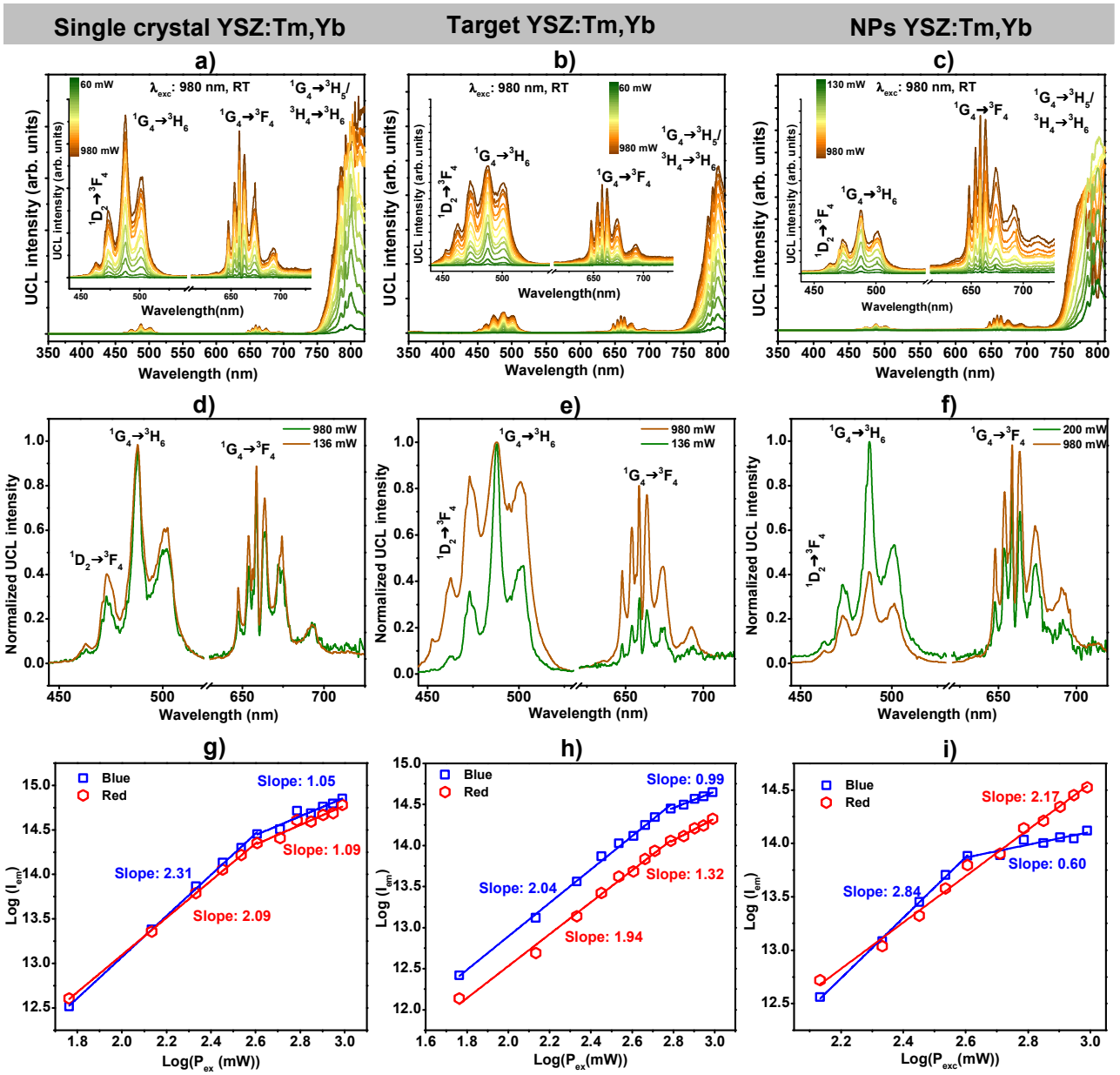

Fig. 6. Dependence of the UCL intensity with the pump power in the YSZ:Tm,Yb single crystal (a), target (b) and NPs (c). d), e) and f) comparison of the visible luminescence upon lower and high power excitation and g), h) and i) linear dependence in a log-log representation of the UCL intensity with the pump power and respective slopes. The measurements were realized with the samples at atmospheric pressure

This effect is much more pronounced for the ceramic target and NPs due to heating effects as discussed later on. In the ceramic target, the increase in power excitation leads to a strong increase of the intensity ratio between the red and blue luminescence, comparatively to the lower power excitation. Moreover, a broadening of the blue emission is also observed for the higher power excitation due to the changes in the relative intensities of the $^1D_2 \rightarrow {}^3F_4$, and $^1G_4 \rightarrow {}^3H_6$ transitions. In the case of the NPs, the increase in the power excitation originates a reversed change in the dominant emission, as seen by the change in the intensity ratio between the red and blue light. For low excitation powers, the UCL intensity (I_{em}) is known to be proportional to the incident excitation power (P_{ex}), $I_{em} \propto P_{ex}{}^n$, where n is the number of infrared photons absorbed per visible photon emitted [34–36].Under such approach a n value of 3 and 4 is expected for the population of the $^1G_4$ and $^1D_2$ multiplets (see Figure 5 c)). The log-log plots of the blue and red integrated UCL as a function of the excitation power for the YSZ:Tm,Yb single crystal, target and NPs samples presented in Figure 6 g), h) and I) show two main regimes. In the first regime, with lower power excitation, both the blue and red light suffer a pronounced increase. A slope of ~2 was

found for the single crystals and targets for both transitions indicating saturation effects in the feeding levels. In the case of the heated NPs, a slope of ~3 reflects the increase in the population of the $^1D_2$ multiplet being, however, accompanied by saturation. The experimental slopes are lower than the expected number of absorbed photons as also documented in literature for different host lattices [35–37], including in co-doped ZrO_2 nanocrystals [38].After a certain power threshold, a second regime is observed. In this higher excitation power regime, the increase of the integrated UCL intensity with the excited power saturates, as evidenced by the calculated slope value (near 1). In the single crystal both blue and red emission follows almost the same trend in both regimes, and no significant changes are observed in the relative emission intensities. In the ceramic target the blue and red UCL intensity follows different trends after the power threshold, evidencing a higher saturation effect for the blue light, explaining the increase in the intensity ratio between the red and blue UCL for higher power excitation.

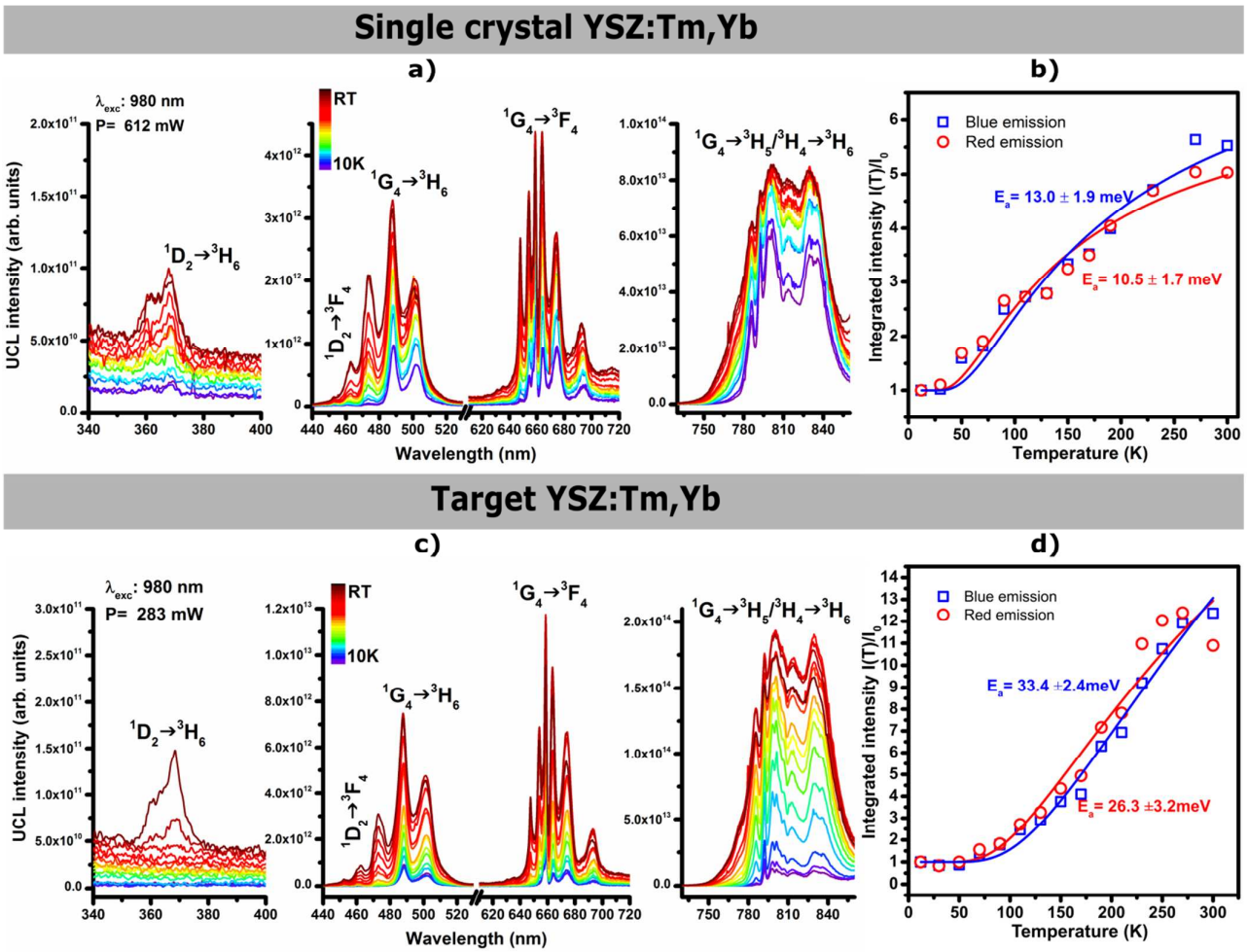

Fig. 7. a) and c) Temperature dependence of the PL spectra, with 980 nm excitation, of the single crystal and target, respectively; b) and d) temperature dependence of the integrated intensity of the red and green emission and respective fit to the *Eq.1* for the single crystal and target, respectively.

The effect of the saturation of the blue light is enhanced in the case of NPs as shown by the slope of ~0.6., explaining the change in the dominant emission colour for the PLAL NPs. Due to the nonlinear effect of the upconversion, for higher power excitation conditions (when the upconversion rates are large) saturation effects are expected, explaining the deviation of the measured *n* values when compared with the predicted ones [34,36,39–41]. Additionally, the nanosized YSZ particles exhibit a higher heating than larger materials resulting in a pronounced saturation effect for higher excitation powers. The temperature dependence of the UCL for the YSZ:Tm,Yb single crystal and target was investigated with the samples in an evacuated cryostat in the temperature range between 12 K to 300 K, as shown in Figure 7. The case of the NPs will be discussed in the next subsection. With the used incident light power, the overall UCL intensity was found to increase with increasing temperatures for both samples, which can be explained by an additional feeding of the emitting levels. Particularly, a notable rise of the intensity of the high energy transitions arising from the $^1G_4$ and $^1D_2$ multiplets is clearly

identified with increasing temperatures. The temperature dependence of the UCL intensity is well accounted for a thermal population law described by a classical Boltzmann distribution defined by the Eq. 1 [42],

$$\frac{I(T)}{I_0} = 1 + C \cdot e^{-\frac{E_a}{k_B(T-T_0)}} \qquad Eq.1$$

where, T is absolute temperature, $I(T)$ and I_0 stands for the UCL integrated intensity at a given temperature T and 12 K, respectively (assuming negligible nonradiative processes at low temperatures), C corresponds to the ratio of the electronic levels effective degeneracies, k_B the Boltzmann constant and E_a to the activation energy for the thermal population. Figure 7 b) and d) displays the dependence of the blue and red UCL integrated intensity with the temperature, with the full lines corresponding to the theoretical fits according to the Eq.1, for the single crystal and target. Activation energies of ca. ~10 meV and 30 meV were obtained to the thermal population of the blue and red emitting states for the single crystal and target, respectively, likely due to phonon absorption/emission energy compensation mechanisms as discussed by Auzel [34,36,39]. The estimated values well match the low energy phonons of the YSZ host (Figure 1), responsible for the material thermal conductivity. For these large sized materials (single crystal and targets) the thermal dissipation process is realized via multiphonon nonradiative processes.

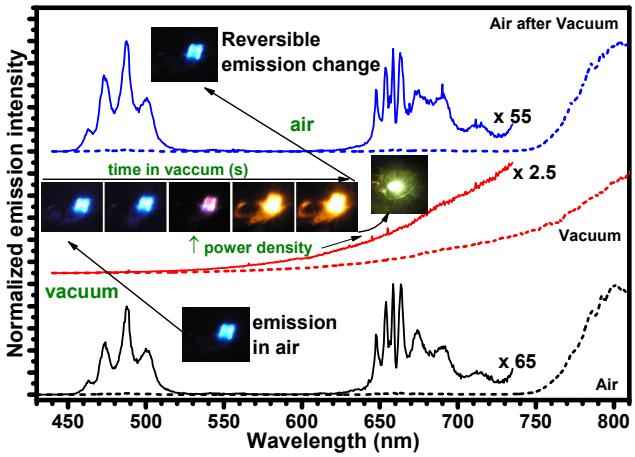

Fig. 8. RT PL spectra of the NPs upon 980 nm excitation performed in air (black lines), in vacuum (red lines) at 10^{-3} mbar and in air after vacuum (blue lines). The dashed lines are the PL spectra in the spectral range between range 440 and 810 nm and the solid lines are magnifications of the same PL spectra in the visible region. Inserted in the figure are photos of the sample when pumped with 980 nm photons in the different atmospheric condition.

Blackbody radiation. Unlike to the observed in single crystal and target, the RT UCL of the NPs was found to be strongly sensitive to the samples environment pressure conditions (air and vacuum, ~10^{-3} mbar) and incident power excitation as shown in Figures 8 and 9. In air, the blue and red NPs UCL (black lines in Figure 8) exhibit the same behaviour of the single crystal and target. Independent of the used incident excitation power the blue UCL is the dominant colour as observed by naked eye. In vacuum, in few seconds, a gradual colour change from the blue to the yellow/orange is observed for the NPs UCL (photos in Figure 8). This effect is totally reversible, with further air replenishments in the cryostat, with a promptly change of the UCL to blue light (upper spectrum, Figure 8), showing a non-contact colour-pressure sensor behaviour. Contrarily to the line spectra measured for the Tm^{3+} intraionic emission, the NPs anti-Stokes radiation measured after few seconds of the samples in vacuum, corresponds to an almost unstructured continuous broad band. The ratio of these two broad band/intraionic anti-Stokes processes was found to be dependent on the used power excitation conditions and materials dimensions as shown in Figures 9 a) and b), being enhanced for the NPs. Particularly, in this case, an increase of the broad band intensity was observed with increasing excitation power. The same effect was observed in minor extent in the ablated area of the targets, whereas no difference was detected for the UCL in single crystals in air and vacuum atmospheres.

These results indicate that the phenomenon is related with the material size reduction, namely with the way how the heat is dissipated on the NPs. It is well established that reducing the material size implies a strong modification on the material physical properties. Particularly, a discrete phonon density of states is expected for the nanocrystals as well as a cutoff of the acoustic phonons [43]. Recently, in distinct classes of undoped and doped nanomaterials with reduced thermal conductivity (YSZ is a thermal barrier coating with typical values of 0.02-0.03 W/cm.K for thermal conductivity [7]), anti-Stokes broad unstructured bands have been reported in different spectral regions [8,19–24,44–50], when the samples are excited with near infrared photons. The anti-Stokes broad band has been discussed on the basis of two main models: blackbody radiation [8,19–24] or photon avalanche mechanism [44–47]. Typically, the emission is enhanced under vacuum conditions. In such reduced pressure conditions, the samples can only dissipate absorbed energy from the incident laser as radiation. On the other hand, for higher pressures, alternative mechanisms of heat dissipation such as gas collisions, results in the quenching of the broad band emission. Accordingly, the emission intensity is expected to decrease exponentially with increasing pressure as identified in several reported papers [19,22,23,45–47]. Low pressures and strong excitations were found to promote the observation of the broad band [8] as identified in our NPs.

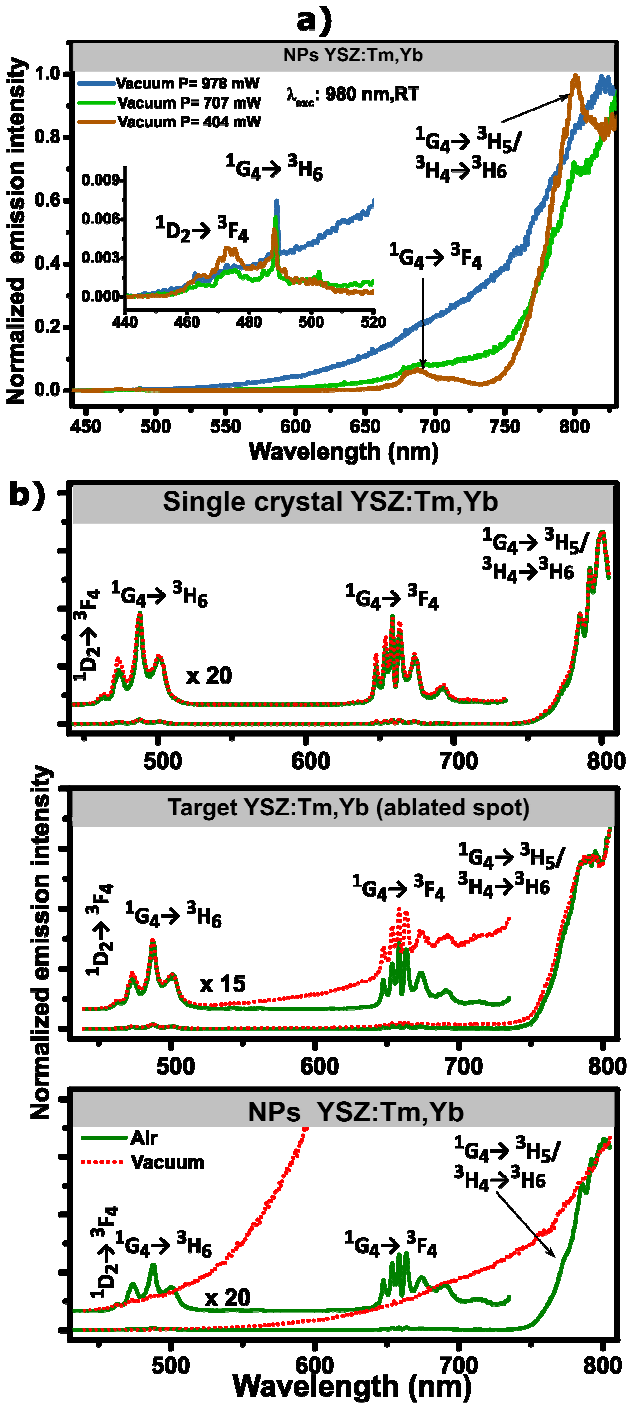

Fig. 9. a) RT PL spectra of NPs, under 980 nm photon excitation, performed in vacuum (10^{-3} mbar) at different power excitation showing the changes in the intensity ratio of the UCL broad band/Tm^{3+} luminescence; b) comparison of the UCL acquired at atmospheric pressure in air and vacuum, for the single crystal, target and NPs.

In order to gain insights on the nature of the anti-Stokes broad band, additional measurements were performed on nominally undoped YSZ and YSZ:Er,Yb NPs with identical dimensions, as shown in Figure 10. As seen, the observation of the broad band is independent of the presence of lanthanide ions (Figure 10 a), b) and c)), suggesting that the observed anti-Stokes band is due to thermal radiation of the NPs. It was also observed that for a fixed incident power the intensity of the unstructured band intensity increases monotonically with increasing wavelength and the band maxima of the emission (limited by the detector cutoff) exhibits a shift to high energies with increasing incident laser power (Figure 10 d)), as expected for a blackbody radiation behavior. A supralinear dependence of the band intensity with the incident power excitation is in fair agreement with other recently published works [19,22]. On the other hand, this model was also supported by the excitation and deexcitation transients of the emitted radiation (Figure 10 e)). As expected for a blackbody radiation the excitation transients evidence a long rise time when compared with the decay lifetime [19]. Figure 10 f) gives additional support for the blackbody radiation model of the anti-Stokes broad band. A near constant intensity of the emission when the cryostat temperature is cooled down from RT to 10 K was observed. As expected, such behavior indicates that the emitted radiation is nearly insensitive to the measured cryostat temperature. Similar findings were reported by the Strek *et al.* [46]. However, in this case the authors assign the broad emission to a CT-lanthanide model supported on photoconductivity data, in analogy with other cases [50].

The high potentialities of the anti-Stokes blackbody radiation appear to be unquestionable. For instance, intense white emission was observed under IR laser excitation in some oxide hosts paving the way for an alternative approach to efficiently generate white light [22,23], displays, IR detection and biosensors. Additionally, in ytterbium doped ZrO_2 host, the harvesting of low-energy solar photons into high energetic ones through thermal radiation with power efficiencies of 16% was recently reported Wang *et al.* [8], opening the way for the use of such radiation in photovoltaic developments. Moreover, and as evidenced in this work, the pressure dependence colour-tuning is of upmost interest for the development of non-contact pressure sensors.

Conclusions

Laser processing technologies were successfully used to produce Tm^{3+} doped and Tm^{3+}, Yb^{3+} co-doped single crystals and NPs by laser floating zone (LFZ) and pulsed laser ablation in liquid (PLAL), respectively. The zirconia additivation with Y^{3+} ions lead to the stabilization of the tetragonal phase of zirconia as observed by Raman spectroscopy. The NPs produced by PLAL have a spherical shape with an average particle diameter of 8.4 nm and are highly crystalline in nature, as observed by HRTEM. The optical activation of the Tm^{3+} ions was achieved in the in-situ doped as-grown single crystals and in the as-produced NPs without the need of further thermal annealing treatments. The downshifted and upconversion luminescence of the doped/co-doped samples was analysed and discussed based on the Tm^{3+} energy schema levels. Intraionic emission in the ultraviolet, blue/green, red and near infrared was observed with resonant excitation conditions into the high energetic multiplets of the Tm^{3+} ions. Additionally, the target

and NPs also exhibit host related Stokes-shifted photoluminescence broad bands. Intense near infrared emission and visible blue light was observed upon infrared excitation and the upconversion emission was investigated as a function of the incident power excitation. The single crystals, target and NPs. Two regimes were found for the blue and red light for single crystals and targets with slopes of ~2 and 1, respectively. The saturation effects were found to be more pronounced for the blue light of the YSZ:Tm,Yb NPs. The temperature dependence of the upconversion luminescence was investigated for single crystals and targets. An overall increase of the integrated intensity was found to be accounted for a thermal activated processes described by activation energies of 10 meV and 30 meV for the single crystal and target, respectively. The estimated energy values are well within the expected values for the low energy phonons in the YSZ host, responsible for the thermal conductivity in large dimension materials. In the case of the NPs, the upconverted luminescence undergoes a change of colour from blue to orange in seconds when the samples are placed in vacuum. Simultaneously, the spectral shape of the emitted radiation in vacuum corresponds to an unstructured wide band starting in the visible and extending to the infrared. The anti-Stokes blackbody radiation was found to be dependent of the incident photon energy power level, pressure and material size dimensions. The effect is enhanced for the nanosized particles as in such case the thermal conduction can be neglected in favour of the thermal radiation. A reversible effect, with a dominant blue light occurs when the NPs are again exposed to air ambience. As shown in the present work, the lanthanide doped YSZ NPs evidence high potentialities for luminescence based sensors aiming biomedical and pressure-based applications. Additionally, the new findings on the continuous upconversion emission are of high importance as alternative approaches for lighting and photovoltaics applications.

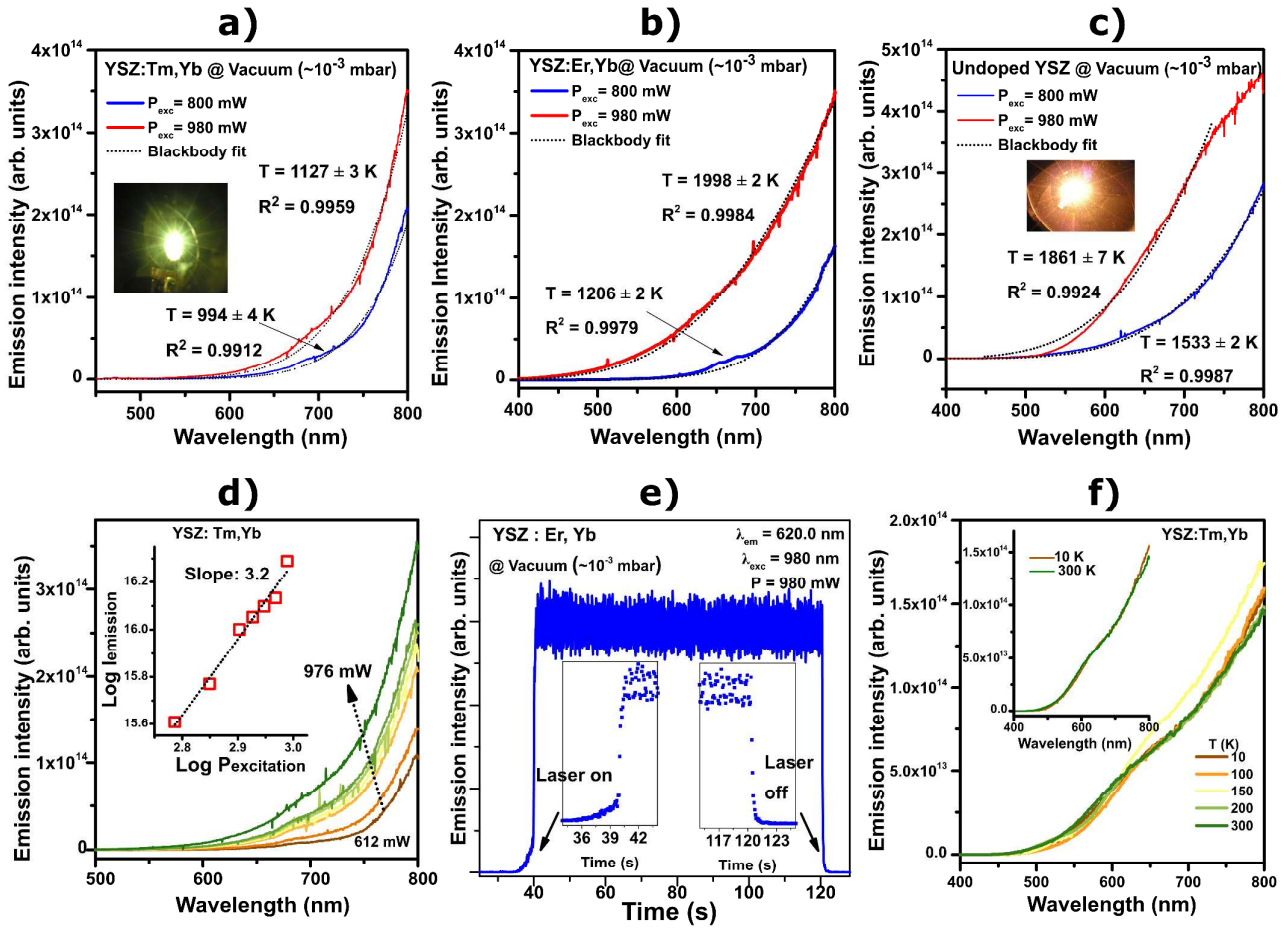

Fig. 10. a),b) and c) Broad emission band acquired under two different infrared laser powers excitation in YSZ:Tm,Yb, YSZ:Er,Yb and YSZ NPs, respectively, produced by PLAL. Black dot curves in the figures represent the fit of the broad emission to the Planck's law of blackbody radiation. The calculated temperatures are indicated in the figures; d) power excitation dependence of the broad emission in the YSZ:Tm,Yb NPs. Inset in the figure shows the excitation power dependence of the integrated broad emission; e) excitation and deexcitation transients of the emitted radiation in the YSZ:Er,Yb NPs; f) temperature dependence of the broad emission band in YSZ:Tm,Yb NPs. Inset in the figure show a comparison between the emission spectra acquired at 10K and 300 K.

Acknowledgements

The authors acknowledge financial support from FCT: UID/CTM/50025/2013, RECI/FIS-NAN/0183/2012 (FCOMP-01-0124-FEDER-027494), and CENTRO-07-ST24-FEDER-002030. M. R. N. Soares thanks to FCT for their PhD grant SFRH/BD/80357/2011. The authors thank Dr. L. Rino for his help in the experiments.

References

1 E. De la Rosa, L. A. Diaz-Torres, P. Salas and R. A. Rodríguez, *Opt. Mater.*, 2005, **27**, 1320–1325.
2 L. A. Diaz-Torres, E. De la Rosa, P. Salas, V. H. Romero and C. Angeles-Chávez, *J. Solid State Chem.*, 2008, **181**, 75–80.
3 J. E. Muñoz-Santiuste, B. Savoini and R. González, *J. Alloys Compd.*, 2001, **323-324**, 768–772.
4 B. Savoini, J. E. Muñoz-Santiuste, R. González, G. K. Cruz, C. Bonardi and R. A. Carvalho, *J. Alloys Compd.*, 2001, **323–324**, 748–752.
5 M. R. N. Soares, M. J. Soares, A. J. S. Fernandes, L. Rino, F. M. Costa and T. Monteiro, *J. Mater. Chem.*, 2011, **21**, 15262–15265.
6 V. H. Romero, E. D. la Rosa, T. López-Luke, P. Salas and C. Angeles-Chavez, *J. Phys. Appl. Phys.*, 2010, **43**, 465105.
7 A. M. Limarga, S. Shian, M. Baram and D. R. Clarke, *Acta Mater.*, 2012, **60**, 5417–5424.
8 J. Wang, T. Ming, Z. Jin, J. Wang, L.-D. Sun and C.-H. Yan, *Nat. Commun.*, 2014, **5**, 5669.
9 H. Dong, L.-D. Sun and C.-H. Yan, *Chem. Soc. Rev.*, 2015, **44**, 1608–1634.
10 Z. Li, A. M. Heidt, J. M. O. Daniel, Y. Jung, S. U. Alam and D. J. Richardson, *Opt. Express*, 2013, **21**, 9289–9297.
11 M. R. N. Soares, L. Rino, F. M. Costa and T. Monteiro, *Phys. Status Solidi B*, 2013, **250**, 815–820.
12 J. Chen and J. X. Zhao, *Sensors*, 2012, **12**, 2414–2435.
13 N.-N. Dong, M. Pedroni, F. Piccinelli, G. Conti, A. Sbarbati, J. E. Ramírez-Hernández, L. M. Maestro, M. C. Iglesias-de la Cruz, F. Sanz-Rodriguez, A. Juarranz, F. Chen, F. Vetrone, J. A. Capobianco, J. G. Solé, M. Bettinelli, D. Jaque and A. Speghini, *ACS Nano*, 2011, **5**, 8665–8671.
14 S. Heer, K. Kompe, H. U. Gudel and M. Haase, *Adv. Mater.*, 2004, **16**, 2102–2105.
15 F. Gonell, M. Haro, R. S. Sánchez, P. Negro, I. Mora-Seró, J. Bisquert, B. Julián-López and S. Gimenez, *J. Phys. Chem. C*, 2014, **118**, 11279–11284.
16 G. Yang, *Laser Ablation in Liquids: Principles and Applications in the Preparation of Nanomaterials*, CRC Press, 2012.
17 P. V. Kazakevich, A. V. Simakin, V. V. Voronov and G. A. Shafeev, *Appl. Surf. Sci.*, 2006, **252**, 4373–4380.
18 T. E. Itina, *J. Phys. Chem. C*, 2011, **115**, 5044–5048.
19 P. Roura, J. Costa, M. López-de Miguel, B. Garrido, J. Fort, J. R. Morante and E. Bertran, *J. Lumin.*, 1998, **80**, 519–522.
20 S. Redmond, *J. Appl. Phys.*, 2004, **95**, 4069.
21 M. L. Debasu, D. Ananias, I. Pastoriza-Santos, L. M. Liz-Marzán, J. Rocha and L. D. Carlos, *Adv. Mater.*, 2013, **25**, 4817–4817.
22 G. Bilir and B. Di Bartolo, *Opt. Mater.*, 2014, **36**, 1357–1360.
23 G. Bilir, G. Ozen, J. Collins, M. Cesaria and B. Di Bartolo, *IEEE Photonics J.*, 2014, **6**, 1–7.
24 W. Chen, Y. Shi, Z. Chen, X. Sang, S. Zheng, X. Liu and J. Qiu, *J. Phys. Chem. C*, 2015, **119**, 20571–20577.
25 M. R. N. Soares, C. Nico, J. Rodrigues, M. Peres, M. J. Soares, A. J. S. Fernandes, F. M. Costa and T. Monteiro, *Mater. Lett.*, 2011, **65**, 1979–1981.
26 M. R. N. Soares, C. Nico, M. Peres, N. Ferreira, A. J. S. Fernandes, T. Monteiro and F. M. Costa, *J. Appl. Phys.*, 2011, **109**, 013516.
27 M. R. N. Soares, T. Holz, F. Oliveira, F. M. Costa and T. Monteiro, *RSC Adv.*, 2015, **5**, 20138–20147.
28 M. R. N. Soares, C. Nico, D. Oliveira, M. Peres, L. Rino, A. J. S. Fernandes, T. Monteiro and F. M. Costa, *Mater. Sci. Eng. B*, 2012, **177**, 712–716.
29 E. F. López, V. S. Escribano, M. Panizza, M. M. Carnasciali and G. Busca, *J. Mater. Chem.*, 2001, **11**, 1891–1897.
30 S. E. Paje and J. Llopis, *Appl. Phys. A*, 1993, **57**, 225–228.
31 H. Nakajima and T. Mori, *J. Alloys Compd.*, 2006, **408-412**, 728–731.
32 F. W. Ostermayer, J. P. van der Ziel, H. M. Marcos, L. G. Van Uitert and J. E. Geusic, *Phys. Rev. B*, 1971, **3**, 2698–2705.
33 F. Pandozzi, F. Vetrone, J.-C. Boyer, R. Naccache, J. A. Capobianco, A. Speghini and M. Bettinelli, *J. Phys. Chem. B*, 2005, **109**, 17400–17405.
34 F. Auzel, *Chem. Rev.*, 2004, **104**, 139–174.
35 S. Xu, W. Xu, Y. Wang, S. Zhang, Y. Zhu, L. Tao, L. Xia, P. Zhou and H. Song, *Nanoscale*, 2014, **6**, 5859–5870.
36 F. E. Auzel, *Proc. IEEE*, 1973, **61**, 758–786.
37 L. An, J. Zhang, M. Liu and S. Wang, *J. Alloys Compd.*, 2008, **451**, 538–541.
38 A. Patra, S. Saha, M. A. R. C. Alencar, N. Rakov and G. S. Maciel, *Chem. Phys. Lett.*, 2005, **407**, 477–481.
39 F. Auzel, P. A. Santa-Cruz and G. F. de Sá, *Rev. Phys. Appliquée*, 1985, **20**, 273–281.
40 M. Pollnau, D. R. Gamelin, S. R. Lüthi, H. U. Güdel and M. P. Hehlen, *Phys. Rev. B*, 2000, **61**, 3337–3346.
41 H. U. Gudel and M. Pollnau, *J. Alloys Compd.*, 2000, **303**, 307–315.
42 C. Nico, R. Fernandes, M. P. F. Graça, M. Elisa, B. A. Sava, R. C. C. Monteiro, L. Rino and T. Monteiro, *J. Lumin.*, 2014, **145**, 582–587.
43 G. Liu and X. Chen, in *Handbook on the Physics and Chemistry of Rare Earths*, ed. J.-C. B. and V. K. P. Karl A. Gschneidner, Elsevier, 2007, vol. 37, pp. 99–169.
44 J.-F. Bisson, D. Kouznetsov, K.-I. Ueda, S. T. Fredrich-Thornton, K. Petermann and G. Huber, *Appl. Phys. Lett.*, 2007, **90**, 201901.
45 J. Wang and P. A. Tanner, *J. Am. Chem. Soc.*, 2010, **132**, 947–949.
46 W. Strek, L. Marciniak, A. Bednarkiewicz, A. Lukowiak, R. Wiglusz and D. Hreniak, *Opt. Express*, 2011, **19**, 14083–14092.
47 L. Marciniak, W. Strek, A. Bednarkiewicz, D. Hreniak, M. C. Pujol and F. Diaz, *J. Lumin.*, 2013, **133**, 57–60.
48 W. Strek, L. Marciniak, P. Gluchowski and D. Hreniak, *Opt. Mater.*, 2013, **35**, 2013–2017.
49 W. Strek, L. Marciniak, D. Hreniak and A. Lukowiak, *J. Appl. Phys.*, 2012, **111**, 024305.
50 C. Brandt, S. T. Fredrich-Thornton, K. Petermann and G. Huber, *Appl. Phys. B*, 2011, **102**, 765–768.